한혁진 교수 지도
석사학위 청구논문

몰리브덴 인화물 단결정 합성법 개발 및 산소환원반응 촉매로의 응용에 대한 연구

Facile Synthesis of Single-Crystal Molybdenum Phosphide as an Electrocatalyst for the Oxygen Reduction Reaction

2025

성신여자대학교 일반대학원
미래응용과학학과
김서현

몰리브덴 인화물 단결정 합성법 개발 및 산소환원반응 촉매로의 응용에 대한 연구

Facile Synthesis of Single-Crystal Molybdenum Phosphide as an Electrocatalyst for the Oxygen Reduction Reaction

한혁진 교수 지도

이 논문을 석사학위논문으로 제출함

2025년 6월

성신여자대학교 일반대학원
미래응용과학학과
김서현

인준서

김서현의 석사학위 논문으로 인준함

2025년 6월

심사위원장 이세현 (서명 또는 인)

심사위원 한혁진 (서명 또는 인)

심사위원 최민재 (서명 또는 인)

성신여자대학교 일반대학원

Abstract

Facile Synthesis of Single-Crystal Molybdenum Phosphide as an Electrocatalyst for the Oxygen Reduction Reaction

Name Seo Hyun Kim
Department Major Next Generation Applied Sciences
Graduate School of
Sungshin Women's University

Hydrogen peroxide (H_2O_2) is widely used in disinfection, water purification, and chemical processing, but its conventional production via the anthraquinone process is energy-intensive and environmentally burdensome. Electrochemical H_2O_2 synthesis via the two-electron oxygen reduction reaction ($2e^-$ ORR) offers a cleaner alternative, yet highly selective and efficient catalysts remain scarce. Molybdenum phosphide (MoP) is a promising candidate due to its electrical conductivity and stability, but traditional synthesis methods yield polycrystalline or amorphous forms with limited facet control. In this study, we developed a liquid-metal-assisted chemical vapor deposition (CVD) strategy using gallium to grow MoP single crystals with controllable facet exposure. By tuning the growth temperature, we selectively obtained (0001) oriented nanoplates and

$(10\bar{1}0)$ oriented pillars. Morphological analyses confirmed high crystallinity and facet definition. Electrochemical tests showed that the $(10\bar{1}0)$ facet exhibited superior H_2O_2 selectivity, attributed to differences in reaction pathways. This work demonstrates a practical synthesis method for facet-controlled MoP crystals, overcoming previous limitations and enabling rational design of MoP electrocatalysts for efficient $2e^-$ ORR-based H_2O_2 production.

Contents

Bibliography

Chapter 1. Introduction

1.1 Necessity of MoP Single-Crystal Synthesis

The growing demand for sustainable energy conversion has accelerated the development of electrocatalysts that are both cost-effective and durable. Among various candidates, transition metal phosphides (TMPs) have garnered considerable attention owing to their earth-abundant composition, tunable electronic structures, and outstanding chemical stability.[1-3] In particular, molybdenum phosphide (MoP) distinguishes itself due to its high thermal and electrical conductivity,[4-6] as well as its excellent catalytic performance in diverse electrochemical reactions such as the hydrogen evolution reaction (HER),[7,8] oxygen evolution reaction (OER),[9,10] and nitrogen reduction reaction (NRR).[11,12]

Structurally, MoP crystallizes in a hexagonal lattice (space group $p\bar{6}m2$), where Mo atoms are coordinated by six phosphorus atoms forming a trigonal prism geometry. This robust crystal structure supports inherent thermal and chemical stability of MoP, while its metallic bonding character accounts for the excellent electrical conductivity observed in bulk and nanostructured forms.

However, most MoP investigations still rely on polycrystalline or amorphous powders whose grain boundaries and random orientations obscure the intrinsic link between surface atomic arrangement and catalytic function, thereby making morphology-driven design exceedingly difficult.[13] Therefore, synthesizing MoP as single crystals, free of grain boundaries and with well defined crystallographic orientations, is crucial for unveiling precise morphology–function relationships and enabling rational catalyst optimization. High quality single crystalline materials offer a precise platform for probing facet defined catalytic behavior, thereby enabling detailed insights into surface-specific reaction pathways.[14]

Traditional approaches for MoP synthesis, including ion-mediated methods, sol

‑ gel methods, and chemical vapor transport (CVT), typically yield polycrystalline or amorphous MoP that are plagued by abundant grain boundaries, morphological defects, and unpredictable facets. These characteristics not only obscure the intrinsic catalytic properties of specific crystal facets but also lead to significant variability across different synthesis batches. For instance, ion-mediated methods suffer from poor control over crystal morphology and often involve leaching of active metal ions, which compromises the chemical stability and limits their reusability in practical applications.[15,16] Sol ‑ gel methods, although useful for achieving homogeneous elemental mixing, frequently produce MoP with low crystallinity and exhibit poor mechanical robustness due to rapid gelation and pore collapse during high-temperature annealing.[17,18] Chemical vapor transport (CVT) methods are known to yield high quality crystals, but they are characterized by extremely slow growth rates, often requiring several days to produce even small domains. Additionally, CVT offers limited scalability and facet control.[19] As a result, it has been challenging to systematically investigate facet-dependent catalytic behavior or to reproducibly synthesize MoP with targeted crystallographic planes.

1.2 Importance of Facet Control in $2e^-$ ORR Catalysis

Hydrogen peroxide (H_2O_2) is a vital chemical widely used in disinfection, bleaching, and water purification, with its global demand steadily increasing. Currently, its industrial production relies heavily on the anthraquinone process, which operates at high temperature and pressure and involves the use of large volumes of organic solvents.[20] This results in substantial energy consumption and raises serious environmental concerns. To overcome these drawbacks, the electrochemical two-electron oxygen reduction reaction ($2e^-$ ORR) has gained attention as a sustainable, decentralized alternative that enables direct H_2O_2 production from O_2 . Although the $2e^-$ ORR pathway for H_2O_2 generation is theoretically efficient, it competes with the thermodynamically and kinetically preferred four-electron pathway leading to water, resulting in a challenging trade-off between selectivity toward H_2O_2 and overall catalytic activity.[21,22]

These performance metrics are highly sensitive to the surface morphology of the catalyst, especially the exposed crystal facets, which govern atomic arrangement, electronic distribution, and the density of active sites. Such factors critically affect the adsorption and desorption energies of key intermediates like OOH*, thereby influencing the preferred reaction pathway. Thus, precise facet control emerges as a crucial strategy for enhancing $2e^-$ ORR performance. Recent studies have demonstrated that the catalytic performance of various metal and TMP based systems is highly sensitive to the specific crystallographic facets exposed, underscoring the critical role of facet engineering in tuning activity and selectivity. In the case of MoP, however, most conventional catalysts consist of amorphous or polycrystalline structures with mixed crystal planes, hindering clear identification and optimization of facet-dependent catalytic behaviors. To overcome this limitation, it is essential to develop MoP materials that expose a single, well-defined crystal facet, thereby enabling enhanced $2e^-$ ORR selectivity and more efficient H_2O_2 electrocatalysis.

1.3 Strategy for Facet Controlled Growth of MoP Single Crystals

In this study, we employed a liquid metal assisted growth strategy to synthesize MoP single crystals with precisely controlled facet exposure. Liquid metals have recently garnered attention as versatile reaction media, owing to their unique physical and chemical properties such as low melting points, high surface tension, and the formation of self-limiting oxide layers.[23-25] These properties enable the controlled synthesis of diverse material systems including high-entropy alloys, two-dimensional materials, and single crystals, with improved yield and accelerated growth rates.[26-28] Gallium, in particular, was chosen as the growth medium because of its negligible solubility for molybdenum, thus promoting highly localized surface reactions and selective exposure of specific crystal facets.[29] Its liquid state also allows precise control of kinetic parameters such as surface diffusion, nucleation, and growth direction by tuning the temperature and precursor flow.[30]

By adjusting growth conditions including temperature, precursor ratio, and phosphorus vapor concentration, we achieved directional crystal growth with improved uniformity. Compared to conventional methods, this process significantly reduces synthesis time and yields crystals with consistent morphology. The surface guided nature of the growth also improves reproducibility across batches. We further regulate phosphorus vapor concentration by adjusting the amount of phosphorus precursor. As summarized in Figure 1, this method provides a reliable and scalable route to grow MoP single crystals with defined surface orientation. It also offers a platform for studying how crystal orientation affects performance in the two-electron oxygen reduction reaction ($2e^-$ ORR), particularly for hydrogen peroxide production.

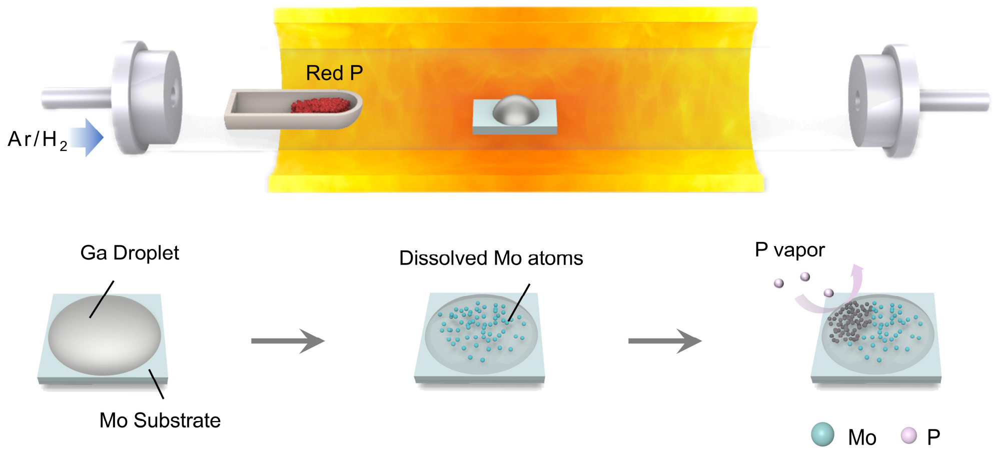

Figure 1

Fabrication process of facet-controlled MoP via liquid gallium-assisted chemical vapor deposition method

Chapter 2. Experimental Section

2.1 MoP Single Crystal Growth via Liquid Metal CVD

Single crystalline molybdenum phosphide (MoP) was synthesized using a liquid-metal-assisted CVD method. Commercial gallium pellets (99.9% purity) were divided into small droplets and deposited onto 1cm×1cm molybdenum (Mo) foils, which served both as the Mo source and the substrate. Red phosphorus powder (99.9% purity) was used as the phosphorus precursor.

The synthesis was conducted in a horizontal tube furnace equipped with a 1 inch diameter quartz tube. A small amount of gallium (0.1-0.2g) was placed on the Mo foil, and the assembly was positioned at the center of the furnace. The phosphorus precursor was loaded into a separate quartz boat located upstream along the gas flow path. During the reaction, a reducing atmosphere was maintained by flowing a mixture of argon (Ar, 250 sccm) and hydrogen (H_2 , 50sccm).

Prior to heating, the system was purged with Ar for 30 minutes to remove residual air. The temperature was then ramped at 30°C/min to the target growth temperature, which was set to either 700°C or 900°C. Simultaneously, the phosphorus precursor was independently heated to 500°C to supply a continuous flux of phosphorus vapor. The reaction was held at the growth temperature for 30 minutes and then rapidly cooled to room temperature under Ar/H_2 flow. All syntheses were performed at atmospheric pressure.

2.2 Physicochemical Characterization of MoP

To characterize the synthesized MoP single crystals, a range of physicochemical analyses was performed. Scanning electron microscopy (SEM) was used to observe surface morphology, while energy-dispersive X-ray spectroscopy (EDS) provided elemental distribution maps. Surface chemical states were analyzed via X-ray photoelectron spectroscopy (XPS) equipped with a monochromatic Al Kα source.

Raman spectra were collected at ambient temperature using a 532nm excitation laser with a beam diameter of 1μm and a ×40 objective lens. The silicon Raman peak at $521cm^{-1}$ served as a calibration reference. Powder X-ray diffraction (XRD) patterns were measured to examine the crystalline structure, and optical absorbance spectra were recorded using an 808nm laser source.

Electron backscatter diffraction (EBSD) analysis was performed to investigate the crystallographic orientation of the samples. Transmission electron microscopy (TEM) was used to examine the crystal structure, while high resolution elemental mapping was carried out using energy dispersive spectroscopy in TEM mode. The elemental composition of Mo, P, and Ga was quantitatively analyzed by inductively coupled plasma mass spectrometry (ICP-MS).

2.3 Electrochemical Analysis on Half Cell

Electrochemical measurements for H_2O_2 production were carried out using a standard three-electrode setup integrated with a rotating ring-disk electrode (RRDE) system and an Autolab potentiostat. A platinum sheet and an Ag/AgCl electrode were used as the counter and reference electrodes, respectively. The working electrode consisted of a glassy carbon disk (area = $0.196cm^2$) with a platinum ring. Prior to each measurement, the working electrode was mechanically polished with alumina powder and rinsed with deionized (DI) water. A catalyst ink was prepared by dispersing 3 mg of the synthesized material in a mixture of isopropanol (0.475μL), deionized water (1.425μL), and 5wt% Nafion solution (50μL), followed by 25 minutes of ultrasonication. The ink was then drop cast onto a glassy carbon electrode at a loading of $20\mu g\cdot cm^{-2}$. After solvent evaporation, a thin catalytic film was formed to facilitate H_2O_2 detection via oxidation at the ring electrode.

Electrochemical pre treatment was conducted by performing 10 cycles of cyclic voltammetry (CV) in an Ar-saturated 0.1M KOH solution with a scan rate of 0.1V/s and a scan range of 0.05-1.0V. The platinum ring surface was simultaneously cleaned by sweeping the potential 20 cycles within the same voltage range at 0.5 V/s. The H_2O_2 production rate and selectivity measurements were performed in an O_2-saturated electrolyte at a scan rate of 0.01V/s and a rotation rate of 1,600 rpm for the disk electrode. The platinum ring electrode was held at 1.2 V (vs. RHE) to oxidize the H_2O_2 produced at the disk. The ORR current was corrected by subtracting the current obtained under Ar-saturated conditions from the current measured in the O_2-saturated electrolyte. Ring current values were adjusted using the RRDE collection efficiency calibrated with a potassium hexacyanoferrate (III) solution (N = 0.278), to enable accurate H_2O_2 quantification. The following equations were used to calculate the collection efficiency, selectivity, $2e^-$ mass activity, TOF, and kinetic current density.

$$Selectivity(\%) = \frac{200 \times (I_r/N)}{(I_d + I_r/N)}$$

$$2e^- \, mass\, activity = \frac{Ring\ \ current\ \ density[A/cm^2]}{Catalyst\, loading\, density\,[g/cm^2]}$$

$$Turnover\, frequency[s^{-1}] = \frac{number\, of\, oxygen\, molecules\, turnover}{number\, of\, active\, sites}$$

$$Number\, of\, oxygen\, molecules\, turned\, over = j\left[\frac{mA}{cm^2}\right] \times \frac{1\left[\frac{C}{S}\right]}{1000[mA]} \times \frac{1[mol\, e^{-1}]}{96485[C]} \times \frac{1[mol\, O_2]}{2[mol\, e^-]} \times (6.02 \times 10^{23}\left[\frac{atom O_2}{Mol O_2}\right]$$

$$Number\, of\, active\, sites = L\left[\frac{mg}{cm^2}\right] \times R[wt\%] \times \frac{1\,[mmol]}{W[mg]} \times (6.02 \times 10^{20}\left[\frac{atom}{mmol}\right])$$

Here, I_r denotes the ring current, I_d represents the disk current, and N denotes the current collection efficiency (0.278). The parameter j refers the H_2O_2 production current density, calculated from the ring current using the RRDE collection efficiency at the specified overpotential. L(0.02 mg/cm^2) denotes the amount of catalyst loaded on the electrode, R(0.244 wt%) represents the weight fraction, and W(30.97 mg) signifies the atomic weight of the active site element.

$$j_k = \frac{j \times j_d}{j_d - j'}$$

$$\frac{1}{j} = \frac{1}{j_k} + \frac{1}{0.62nFC_0(D_0)2/3v^{-1/6}w^{1/2'}}$$

Here, j_k is the kinetic current density, while j is the experimentally measured current density. The term w refers to the angular rotation speed of the electrode. n denotes the number of electrons transferred per O_2 molecule, and F is the Faraday constant (96,485 C·mol^{-1}). C_0 indicates the concentration of dissolved O_2 in the electrolyte at room temperature (1.1×10^{-6} mol·cm^{-3}), D_0 is the diffusion coefficient of O_2 in the electrolyte (1.9×10^{-5} cm^2·s^{-1}), and v corresponds to the kinematic viscosity of the electrolyte at 25 °C (1.0×10^{-2} cm^2·s^{-1}).

The electrochemically active surface area (ECSA) was evaluated based on the double-layer capacitance (C_{dl}). To exclude interference from residual oxygen, cyclic voltammetry was performed in the non-Faradaic region using Ar-saturated 0.1M KOH at scan rates of 60, 80, 100, 120, 140, and 160 mV·s^{-1}. By plotting △j as a function of scan rate, the resulting slope – corresponding to C_{dl} – was used to determine the ECSA, given their linear relationship. The ECSA was then calculated using the following equations:

$$ECSA = \frac{C_{dl}}{C_s} \times A_{GCE}$$

Here, C_S refers to the specific capacitance of the electrode surface, and A_{GCE} represents an electrode surface area.[31-33] A commonly used C_S value of 40·µF cm^{-2} was employed for the ECSA calculation

2.4 Accumulated H_2O_2 Measurement in H-cell System

Electrocatalytic H_2O_2 production was evaluated using a Teflon treated carbon fiber paper loaded with the catalysts in a two compartment H-cell system with a Nafion 117 membrane as the separator. A graphite rod and an Ag/AgCl electrode were used as the counter and reference electrodes, respectively. And MoP pillar modified carbon fiber paper (0.5×0.5 cm^2) as the WE, with a mass loading rate of $0.1 mg\cdot cm^{-2}$. Both compartments (50mL each) were filled with the same electrolyte.

The concentration of produced H_2O_2 concentration was quantified via a colorimetric method. To construct a calibration curve, standard H_2TiO_4 solutions were prepared by treating H_2O_2 solutions (concentration range: 0.1-4.0 mM) with 3.8mL of 0.1M acidified titanium sulfate. The absorbance of these solutions was measured at 407nm using a ultraviolet visible spectrophotometer, revealing a linear correlation between absorbance and H_2O_2 concentration within the tested range. The resulting calibration curve was applicable to acidified titanium sulfate solutions over this concentration range. To quantify H_2O_2 in the electrolyte, 0.2mL of the sample was mixed with 3.8mL of 0.1M acidified titanium sulfate, and the absorbance was evaluated against the calibration curve. The total charge flux through the electrode was integrated over time, confirming high Faradaic efficiency for both instantaneous and sustained H_2O_2 production under chronoamperometric conditions. These results highlight the system's potential for long-term H_2O_2 electrosynthesis.

H_2O_2 productivity was calculated using the following equations:

$$FE = 2 \times C_{H_2O_2} \times F \times \frac{V}{Q} \times 100\%$$

$$H_2O_2\, productivity\, [mmol\, h^{-1} g^{-1}] = C_{H_2O_2} \times V \times \frac{10^3}{A \times m \times t'}$$

Here, $C_{H_2O_2}$ denotes the concentration of H_2O_2 (0.00035797 $mol\cdot L^{-1}$), F is the

Faraday constant (96485.3 C/mol), and V denotes the volume of electrolyte used (0.5 L), Q represents the accumulated charge (4.70208 C), A corresponds to the electrode surface area (0.5 cm^2), m indicates the catalyst mass loading (0.1 mg cm^{-2}), and t refers to the reaction time (1h).

2.5 Computational Details

All density functional theory (DFT) calculations were performed using the Vienna Ab initio Simulation Package.[34-36] The exchange–correlation energy is described using the Perdew–Burke–Ernzerhof[37] functional within the generalized gradient approximation framework.[38] The electron–ion interactions were modeled using projector augmented-wave (PAW) pseudopotentials.[39] The Mo $4s^24p^64d^55s^1$, P $3s^23p^3$, O $2s^22p^4$, and H $1s^1$ electrons were explicitly treated as valence states. A plan-wave basis set was applied, and the kinetic energy cutoff was set at 500eV. The convergence criteria for total electronic energy and morphological optimization forces were set to 10^{-6}eV and 0.02eV·$Å^{-1}$, respectively. Brillouin zones were sampled using a 12×12×9 Monkhorst Pack k-point grid for bulk models and a 3×3×1 grid for slab models.[40]

To calculate surface free energies, asymmetric slab models were constructed by fixing the bottom atomic layers and allowing relaxation of the upper layers. This approach follows a modified procedure adapted from previous literature.[41] Surface energies (γ) were computed using the following expression:

$$\gamma = \frac{E_{cle} + E_{rel}}{A}$$

$$E_{cle} = \frac{E_{unrelax} - N_{MO} \times E_{bulk} - (N_{MO} - N_P) \times \mu_P}{2}$$

If the surface is symmetric (e.g., (0001) and $(10\bar{1}1)$), we have

$$E_{rel} = \frac{E_{relax} - E_{unrelax}}{2}$$

If the surface is asymmetric (e.g., $(10\bar{1}0)$), we have

$$E_{rel} = E_{relax} - E_{unrelax}$$

In these equations, $E_{unrelax}$ and E_{relax} refer to the total energies of the unrelaxed and partially relaxed MoP surfaces (upper half), respectively. A indicates the surface area of the slab, N is the number of atoms, and μ denotes the chemical potential. For slab construction, the (0001) and $(10\bar{1}0)$ facets were modeled with nine atomic layers, fixing the bottom three layers, whereas the $(10\bar{1}1)$ facet was composed of five layers with the bottom two layers constrained. A vacuum spacing of 15Å was introduced along the surface normal to avoid spurious interactions between periodic images.

The diffusion energy barrier for a Mo adatom on the MoP (0001) facet was computed using the climbing image nudged elastic band (CI-NEB) method, employing a spring constant of -5.0 eV·Å^{-2} and a force convergence threshold of 0.05 eV·Å^{-1}. To simulate adatom migration across surface features, a stepped (0001) facet of MoP slab model was constructed. The energy profile of Mo adatom diffusion was obtained by interpolating several intermediate configurations between the initial and final adsorption sites.

The 2e^{-} pathway of the ORR, which leads to H_2O_2 production, involves the following reactions.

$$* + O_2(g) + H^+ + e^- \rightarrow {*OOH}$$

$$*OOH + H^+ + e^- \rightarrow H_2O_2(g)$$

Conversely, the 4e^{-} pathway of the ORR in an acidic solution proceeds as follows.

$$* + O_2(g) + H^+ + e^- \rightarrow {*OOH}$$

$$*OOH + H^+ + e^- \rightarrow {*O} + H_2O$$

$$*O + H^+ + e^- \rightarrow {*OH}$$

$$*OH + H^+ + e^- \rightarrow H_2O(l)$$

The adsorption energy was calculated using the following equation:

$$E_{ads} = E^{tot}_{surface+adsorbate} - E^{tot}_{surface} - \mu_{adsorbate}$$

Here, $E^{tot}_{surface+adsorbate}$, $E^{tot}_{surface}$, and $\mu_{adsorbate}$ refer to the total energy of the surface slab with the adsorbate, the total energy of the clean surface slab, and the chemical potential of the adsorbed species, respectively.

The Gibbs free energy of adsorption (ΔG_{ads}) was subsequently determined using the following relation:

$$\Delta G_{ads} = E_{ads} + \Delta ZPE - T\Delta S$$

In this equation, E_{ads} is the adsorption energy, and ΔZPE represents the difference in zero-point energy between the adsorbed and gas phase states, T is the temperature, and ΔS is the corresponding entropy change. The zero-point energy and entropy values were obtained from DFT calculations conducted at ambient conditions.

Chapter 3. Result

3.1 Engineering Facets of Single-Crystalline MoP

MoP single crystals showed a clear temperature-dependent difference in morphology and facet orientation. At 900°C, the crystals grew predominantly along the (0001) direction, forming flat hexagonal nanoplates. In contrast, growth at 700°C favored the $(10\bar{1}0)$ orientation, leading to vertically aligned hexagonal pillars. Nanoplates synthesized at 900°C exhibited an average lateral size of 139.92μm (± 32.85μm) and a thickness of 807nm (± 110nm), whereas pillars grown at 700°C had significantly smaller lateral widths of 27.3μm (± 2.64μm) but substantially greater vertical thicknesses of 63.50μm (± 10.70μm). Interestingly, an intermediate morphology was observed when the synthesis was carried out at 800°C. Under this condition, MoP crystals adopted a truncated pyramid shape that combines morphological characteristics of both nanoplates and pillars. This suggests a transitional regime in which the balance between lateral and vertical growth is delicately maintained.

This morphological evolution is closely governed by temperature-dependent surface diffusion dynamics. Elevated temperatures enhance atomic mobility, facilitating lateral expansion along planes parallel to the substrate, which leads to dominant exposure of the (0001) facet. In contrast, reduced atomic diffusion at lower temperatures directs crystal growth along the [0001] axis, resulting in sidewall exposure of the $(10\bar{1}0)$ facet. These growth directions reflect a competition between thermodynamically stable low-energy facets and kinetically favored high-index planes, where high temperatures enable the system to approach its equilibrium morphology. The SEM images of the three representative morphologies—pillar, pyramid, and nanoplate—are collectively presented in Figure 2, which visually captures the temperature-dependent evolution of MoP crystal shapes.

The theoretical basis for these facet dependent growth behaviors, including surface energetics and diffusion barriers, is discussed in detail in Section 3.4. These findings highlight the critical role of synthetic temperature in directing facet exposure during MoP single crystal growth. This tunability enables controlled access to specific surface terminations that directly influence catalytic site accessibility and intermediate binding strength in electrocatalytic reactions.[42] Facet selective growth, driven by surface kinetics, thus provides a rational and scalable route to tailoring the morphology and performance of transition metal phosphides. Such precise control over crystal morphology not only enhances intrinsic reactivity but also offers a pathway to improved mechanical and chemical stability by reducing the incorporation of high energy morphological defects.[43]

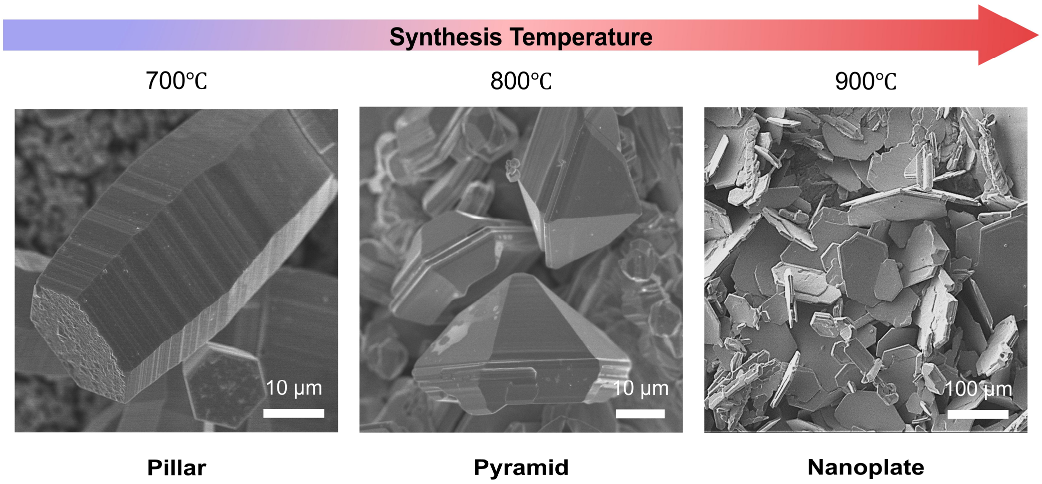

Figure 2

SEM images show the temperature-dependent morphology of MoP single crystals, with hexagonal pillars formed at 700°C, truncated pyramids at 800°C, and flat nanoplates at 900°C.

3.2 Physicochemical Characterization

A comprehensive physicochemical analysis was conducted to evaluate the crystallinity, facet orientation, and atomic scale morphological integrity of the synthesized MoP single crystals. High resolution transmission electron microscopy (HRTEM) and selected area electron diffraction (SAED) were first employed to assess the internal crystallographic order and phase purity of both nanoplates and pillars.

As shown in Figure 3, both morphologies exhibited clear and periodic lattice fringes, indicative of high crystallinity. For the MoP nanoplate, HRTEM analysis revealed a vertical growth axis predominantly oriented along the $(10\bar{1}0)$ plane, with a measured lattice spacing of approximately 0.28nm, which corresponds well to the theoretical interplanar distance of the $(10\bar{1}0)$ planes. In addition, HRTEM images also displayed lattice spacings of 0.32nm, consistent with the (0001) planes. The associated SAED patterns exhibited well defined diffraction spots with hexagonal symmetry along the $[10\bar{1}0]$ and [0001] zone axes, respectively, conclusively confirming the single crystalline nature and crystallographic orientation of the samples.

To further verify the surface facet exposure of the two morphologies, electron backscatter diffraction (EBSD) mapping was performed. As illustrated in Figure 4, the nanoplates were found to predominantly expose the (0001) basal facet, whereas the pillars were characterized by vertical sidewalls with a dominant exposure of the $(10\bar{1}0)$ facet. This distinct facet orientation is consistent with the temperature dependent facet selective growth behavior observed during the synthesis process, further supporting the facet engineering achieved in the MoP crystal system.

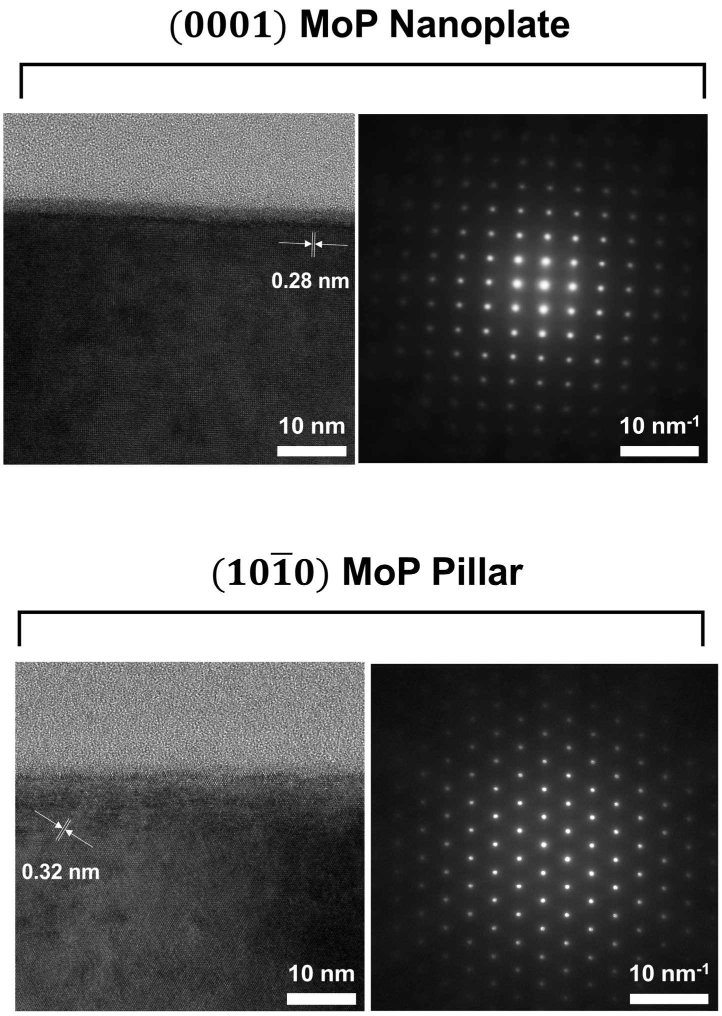

(0001) MoP Nanoplate

$(10\bar{1}0)$ MoP Pillar

Figure 3

HRTEM and SAED analyses confirm the high crystallinity and single crystal MoP nanoplates and pillars, showing well-defined lattice fringes and zone axis diffraction patterns corresponding to the expected crystallographic planes.

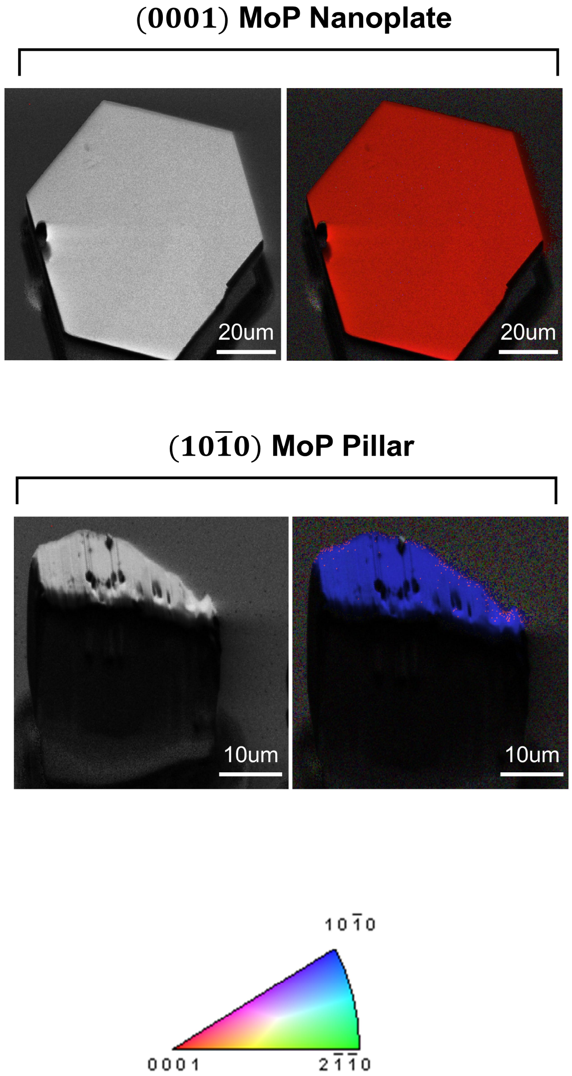

(0001) MoP Nanoplate

$(10\bar{1}0)$ MoP Pillar

Figure 4

EBSD mapping reveals dominant facet exposure of the (0001) plane in nanoplates and the $(10\bar{1}0)$ plane in pillars, consistent with temperature-dependent facet-selective growth.

The overall phase purity and crystallinity of the MoP single crystals were validated by powder X-ray diffraction (XRD). All diffraction peaks were indexed to the hexagonal MoP phase (space group: $p\bar{6}m2$), with no evidence of secondary phases such as MoO_x or MoP_2. The XRD patterns shown in Figure 5a exhibit intense reflections, indicative of high morphological order. Energy dispersive X-ray spectroscopy (EDS) analysis confirmed the elemental composition of the synthesized MoP crystals, revealing a uniform distribution of Mo and P across both nanoplates and pillars with no detectable contamination from oxygen or gallium. The Mo:P atomic ratio was found to be close to 1:1, consistent with stoichiometric MoP. This result was further supported by the close overlap between the EDS spectra of the synthesized crystals and that of a reference MoP bulk crystal grown via CVT method, as shown in Figure 5b. The absence of Ga signals from EDS spectra further confirms that Ga, used as the liquid growth medium, does not incorporate into the MoP lattice. ICP-MS analysis revealed trace Ga impurities of 518.16 ppm, higher than commercial MoP powder (16.03 ppm), yet sufficiently low to suggest that further optimization of etching conditions could reduce impurities, as detailed in the Table 1.

Vibrational and chemical bonding characteristics were also investigated. Raman spectra revealed a single phonon mode in both morphologies, consistent with bulk MoP reference data, as shown in Figure 6a. X-ray photoelectron spectroscopy (XPS) measurements further confirmed the formation of Mo–P bonds and the chemical stability of the material, with well-defined Mo 3d and P 2p peaks identified in the spectra presented in Figures 6b and 6c.

These combined morphological and compositional analyses confirm that the synthesized MoP single crystals exhibit high phase purity, well-defined crystallographic orientation, and excellent material quality, providing a robust foundation for subsequent electrochemical evaluation.

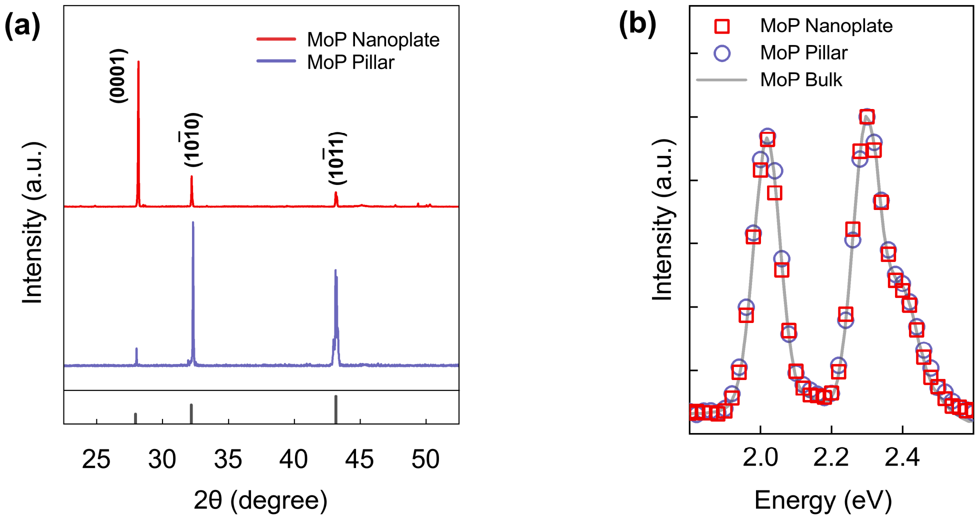

Figure 5

(a) XRD patterns of MoP single crystals show sharp reflections indexed to the hexagonal MoP phase with no detectable secondary phases. (b) EDS spectra confirm stoichiometric Mo:P atomic ratios and compositional consistency with reference MoP crystals, with no detectable Ga incorporation.

	Mo (mg/Kg)	P (mg/Kg)	Ga (mg/Kg)
MoP Single Crystal	860213.550	145184.744	518.166
Commercial MoP (99.5%)	868850.359	148386.143	16.032

Table 1
ICP-MS analysis reveals trace Ga impurities in the synthesized MoP crystals, at higher levels than commercial MoP powder but sufficiently low to suggest minimal incorporation into the crystal lattice.

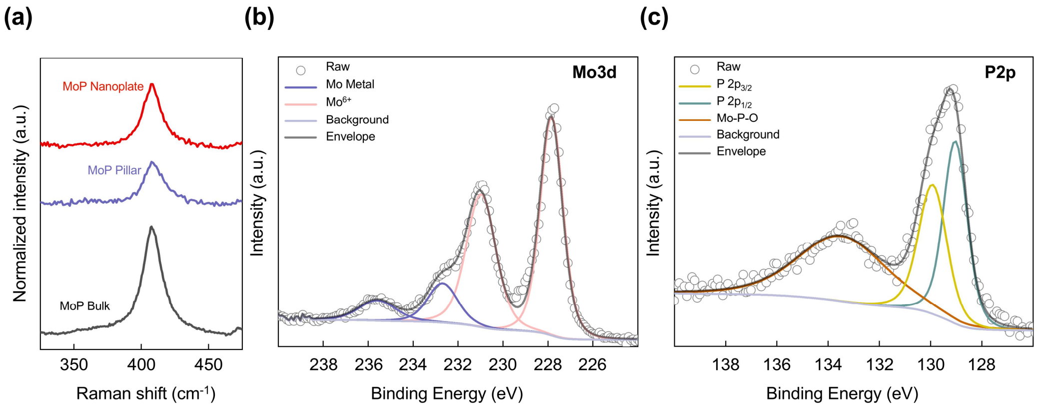

Figure 6

(a) Raman spectra exhibit a single phonon mode consistent with bulk MoP. (b) XPS Mo 3d spectrum shows well-defined peaks corresponding to Mo–P bonding states. (c) XPS P 2p spectrum confirms the chemical stability and proper bonding environment of phosphorus in the MoP lattice.

3.3 Electrochemical Performance on Half Cell

To evaluate the facet dependent electrocatalytic activity of MoP single crystals toward the $2e^-$ ORR, rotating ring disk electrode (RRDE) measurements were conducted in O_2-saturated 0.1 M KOH electrolyte at room temperature. Both MoP nanoplates which predominantly expose the (0001) facet, and MoP pillars characterized by exposure of the $(10\bar{1}0)$ facet, were tested under identical conditions. The use of single crystalline catalysts allows the elimination of grain boundary effects and heterogeneity, providing a direct probe of facet specific catalytic activity. This approach has previously been shown to reveal true morphology-activity relationships in TMP catalysts. In particular, the two facets investigated here, (0001) and $(10\bar{1}0)$, represent contrasting surface terminations with distinct coordination environments, which can drastically alter O_2 adsorption and intermediate desorption energies.[44]

3.3.1 RRDE Performance and H_2O_2 Selectivity

The corresponding disk and ring current profiles revealed a clear morphological dependence in $2e^-$ ORR activity. As illustrated in Figure 7a, the MoP pillars exhibited substantially greater H_2O_2 detection current at the ring electrode than the nanoplate, indicating superior $2e^-$ pathway selectivity associated with the $(10\bar{1}0)$ facet. This enhancement suggests more effective OOH* intermediate desorption and suppression of further reduction to H_2O, thereby promoting selective H_2O_2 formation. To reinforce this facet-dependent interpretation, an additional experiment was conducted using a polycrystalline MoP sample containing a random distribution of crystallographic planes. Figure 7a also shows that the polycrystalline sample exhibited lower H_2O_2 currents compared to the MoP pillar, despite possessing comparable or slightly higher geometric current than the nanoplate. This outcome excludes surface complexity or grain boundary effects as dominant contributors, and instead emphasizes the intrinsic influence of the exposed crystallographic facet. The result from the polycrystalline sample thus serves as a supplementary comparison that further validates the conclusion that the enhanced electrocatalytic performance of the MoP pillars originate from its well-defined $(10\bar{1}0)$ surface.

At 0.45 V (vs. RHE), the MoP pillars delivered a ring current of $1.28\mathrm{mA\cdot cm^{-2}}$, substantially greater than that of the nanoplates ($0.49\mathrm{mA\cdot cm^{-2}}$). The corresponding H_2O_2 selectivity, as shown in Figure 7b, was highest for the pillars, achieving over 92% selectivity, notably higher than that observed for the nanoplates. These results suggest that the $(10\bar{1}0)$ facet provides a more favorable surface environment for selective H_2O_2 formation via the $2e^-$ pathway.

This high selectivity is consistent with the idea that the $(10\bar{1}0)$ facet enables moderate binding of OOH intermediates, facilitating their desorption as H_2O_2 before over reduction to H_2O occurs. Such behavior is aligned with volcano type trends observed in ORR catalysis, where binding strength must be balanced between adsorption and desorption.

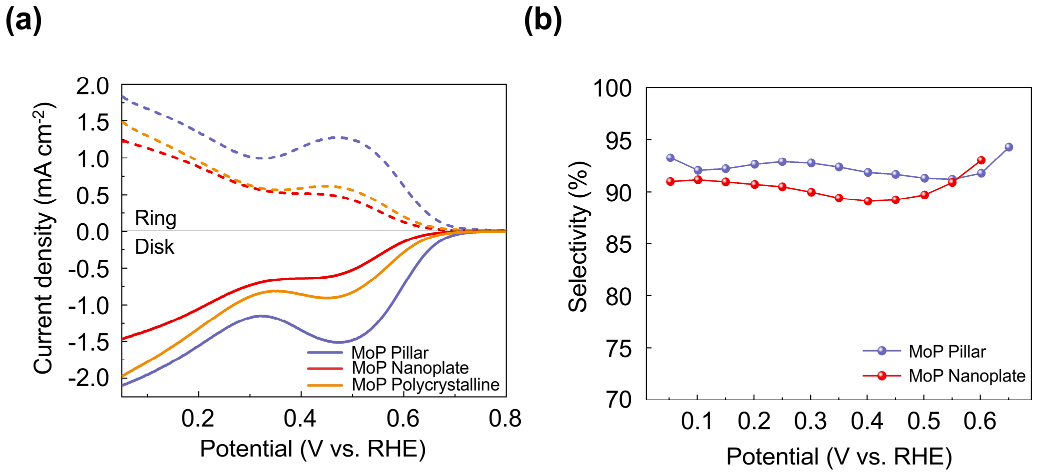

Figure 7

Electrochemical ORR performance for H_2O_2 production based on the exposure of different crystal facets of MoP single crystals. (a) RRDE measurements comparing ORR activity and H_2O_2 ring current densities for MoP pillars, nanoplates, and a polycrystalline sample in O_2-saturated 0.1 M KOH at a sweep rate of 10 mV/s. MoP pillars exhibit the highest ring current, indicating enhanced $2e^-$ pathway selectivity. (b) Comparison of H_2O_2 selectivity at 0.45 V vs. RHE, showing over 92% selectivity for MoP pillars, substantially higher than that of nanoplates.

3.3.2 Kinetic Current Density and Tafel Analysis

To understand the origin of the enhanced performance observed in the MoP pillars, the kinetic current density (j_k) was calculated using the Koutecky–Levich equation to eliminate mass transport effects. At 0.45 V vs. RHE, the MoP pillars exhibited a j_k value of $2.85 mA\cdot cm^{-2}$, markedly higher than the $0.77\ mA\cdot cm^{-2}$ obtained for the nanoplates, as shown in Figure 8a. Moreover, the onset potential for ORR was more positive for the pillars (0.68 V vs. RHE) than for the nanoplates (0.61 V vs. RHE), indicating a more energetically favorable pathway. These trends were consistently observed in tests including polycrystalline MoP, as also shown in Figure 8a, where the pillar morphology demonstrated both the highest j_k and the most positive onset potential.

Tafel slope analysis further elucidated the reaction kinetics. As illustrated in Figure 8b, the MoP pillars exhibited a Tafel slope of $84.4\ mV\cdot dec^{-1}$, significantly lower than the $123.5\ mV\cdot dec^{-1}$ observed for the nanoplates. This result suggests a more favorable electron transfer process for the $(10\bar{1}0)$ facet. The same facet related enhancement was reflected in the mass transfer corrected Tafel slopes for polycrystalline MoP, reinforcing the role of the $(10\bar{1}0)$ surface in promoting accelerated $2e^{-}$ ORR kinetics.

The turnover frequency (TOF) also supported the superior catalytic behavior of the pillars. The TOF of MoP pillars reached $0.04 s^{-1}$, which is 2.5 times greater than the $0.016 s^{-1}$ measured for the nanoplates, as shown in Figure 8c. This indicates a higher intrinsic catalytic rate at the active sites for the pillars.

Finally, the superior performance of the pillars in practical terms is reflected in their mass activity. As shown in Figure 8d, the MoP pillars exhibited consistently higher mass activity over the full potential range of 0.05–0.55 V vs. RHE compared to nanoplates and polycrystalline MoP. This highlights their strong applicability in energy devices requiring efficient oxygen reduction performance.

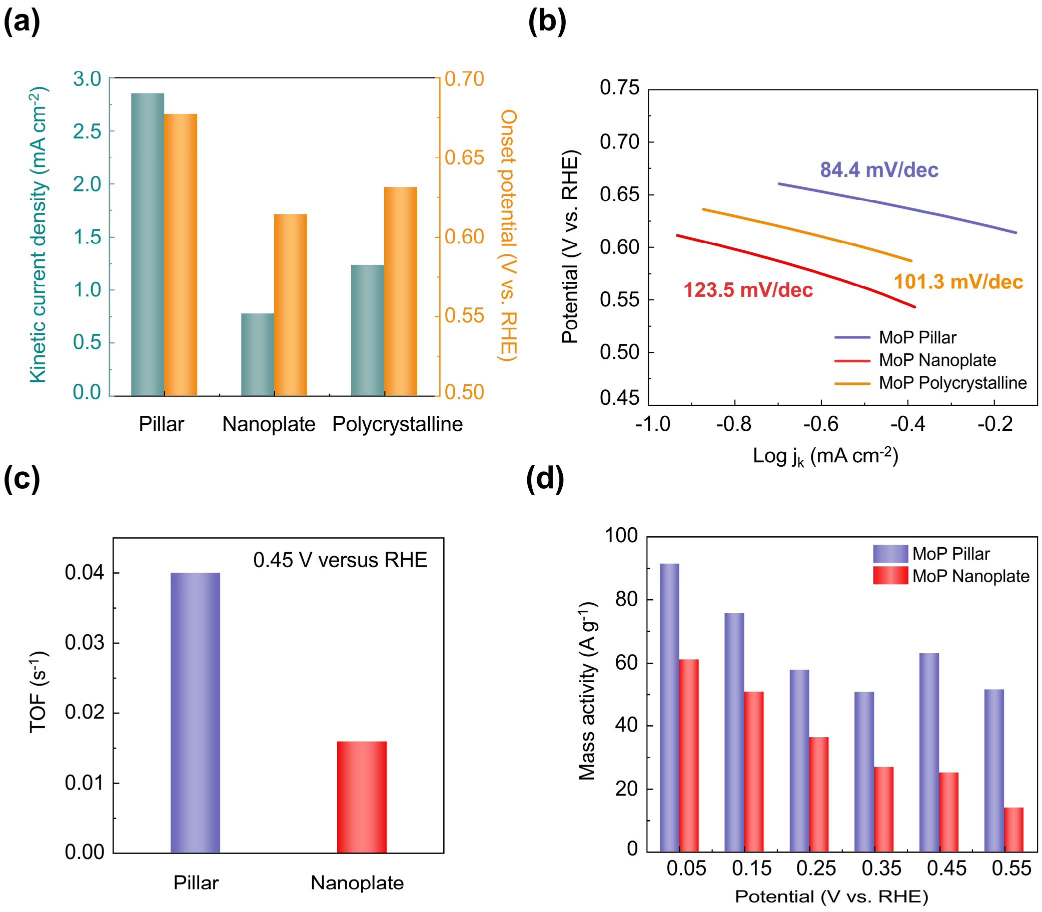

Figure 8

Electrochemical characterization of MoP single crystals for $2e^-$ ORR. (a) Kinetic current density and onset potential for pillar, nanoplate, and polycrystalline samples based on Koutecky‑Levich analysis. (b) Mass transfer corrected Tafel slopes comparing the three morphologies. (c) Turnover frequency (TOF) comparison between MoP pillars and nanoplates. (d) Mass activity curves for MoP pillars and nanoplates over the potential range of 0.05‑0.55 V vs. RHE.

3.3.3 ECSA-Normalized Intrinsic Activity

The MoP pillar exhibited a greater electrochemically active surface area (ECSA) than the nanoplate, as indicated by their higher double layer capacitance (Cdl) values of 9.52 and 7.04 μF·cm^{-2}, respectively. These values, determined from the slopes of the non-Faradaic current versus scan rate plots, are derived from cyclic voltammetry (CV) measurements conducted over a potential window of 0.7 - 0.8 V vs. RHE at scan rates ranging from 60 to 160 mV·s^{-1}, as shown in Figure 9a-c. When the linear sweep voltammetry (LSV) curves were normalized to ECSA, the ORR current density at 0.45 V vs. RHE was approximately 1.8 times higher for the MoP pillar than for the nanoplate, as demonstrated by the ECSA-normalized LSV profiles in Figure 9d, confirming their superior intrinsic catalytic activity.

Compared to polycrystalline MoP, which contains a mixture of exposed crystal planes, the single crystalline MoP pillar demonstrated markedly enhanced H_2O_2 production. Although the polycrystalline sample showed a slightly higher geometric current than the nanoplate, its larger ECSA of 14.2 μF·cm^{-2} did not lead to improved intrinsic performance. The relevant CV curves and ECSA estimation are shown in Figure 10. In fact, its ECSA-normalized ORR activity was lower than that of both the nanoplate and the pillar.

These results highlight that maximizing surface area alone is insufficient; instead, catalytic performance is primarily governed by the precise crystallographic nature of the exposed surface. The enhanced activity observed in the pillars underscores this point, as facet specific electronic and geometric effects can significantly influence reactivity and are only accessible through controlled single crystal synthesis.

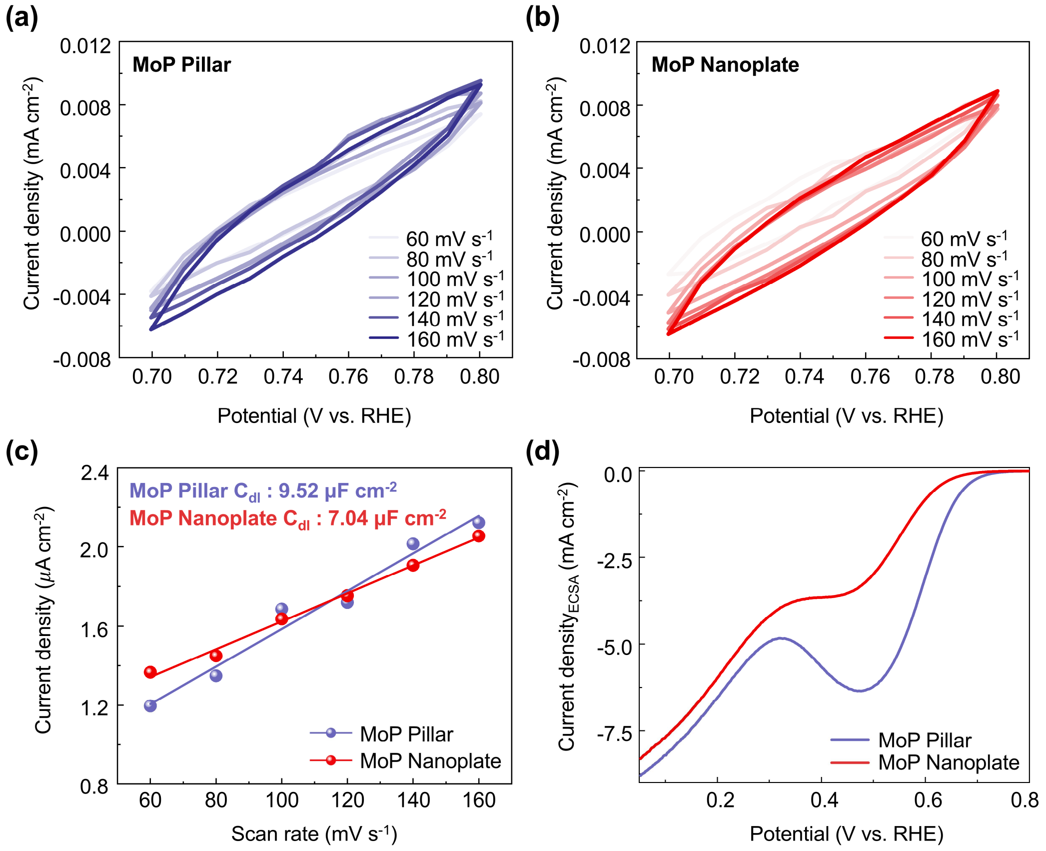

Figure 9

(a, b) CV curves of the MoP pillar (a) and the nanoplate (b) at the scan rates ranging from 60 mV s^{-1} to 160 mV s^{-1} within a potential window of 0.7 V–0.8 V (vs. RHE). (c) The double-layer capacitance (Cdl) determined from the CV curves. (d) The LSV curves normalized by ECSA.

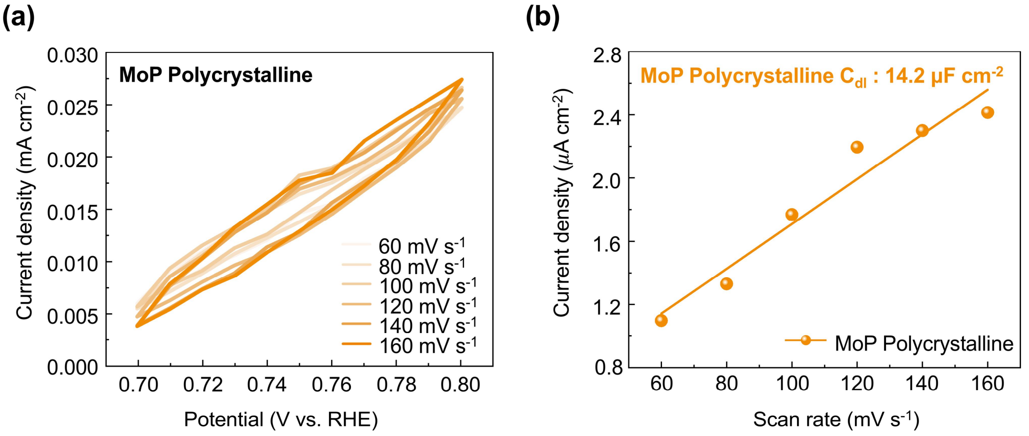

Figure 10

CV curves at different scan rates and the calculated ECSAs. (a) The CV curves were measured at the scan rates of 60 mV s^{-1} to 160 mV s^{-1} in the potential window of 0.7 V–0.8 V (vs. RHE) for the polycrystalline MoP. (b) According to the double-layer capacitance (C_{dl}) method based on the CV curves, the ECSAs can be calculated.

3.3.4 Continuous H_2O_2 Electrosynthesis and Stability

MoP Pillars exhibited excellent performance in continuous H_2O_2 electrosynthesis under O_2-saturated alkaline conditions. A steady state current density of approximately −3.5 $mA \cdot cm^{-2}$ was maintained at 0.1 V vs. RHE for over 80 hours without noticeable degradation. Concurrently, the H_2O_2 concentration in the electrolyte increased progressively, reaching 7.6 mM after 10 hours of electrolysis, while the Faradaic efficiency remained above 90% throughout the test.

The electrocatalytic stability and yield behavior are illustrated in Figure 11. Figure 11a presents the H_2O_2 yield rate and Faradaic efficiency across a potential window of 0.1 - 0.5 V, where the yellow coloration from the reaction with $TiOSO_4$ confirms effective H_2O_2 generation. Figure 11b compares the theoretical H_2O_2 yield calculated from chronoamperometric data with the experimentally detected concentration and efficiency over a 20 hours period, revealing a maximum yield rate approaching 359.97 mmol $g^{-1}h^{-1}$. The inset image highlights the progressive color change during electrolysis. Long-term durability is further demonstrated by the chronoamperometry profile in Figure 11c, showing stable current output over 28 hours at 0.1 V.

These results demonstrate that the MoP pillar catalyst not only enables high activity and selectivity for the two-electron oxygen reduction reaction, but also maintains morphological integrity and electrochemical stability during extended operation. The consistently high Faradaic efficiency and long term durability further underscore the strong potential of this system for practical and decentralized H_2O_2 production.

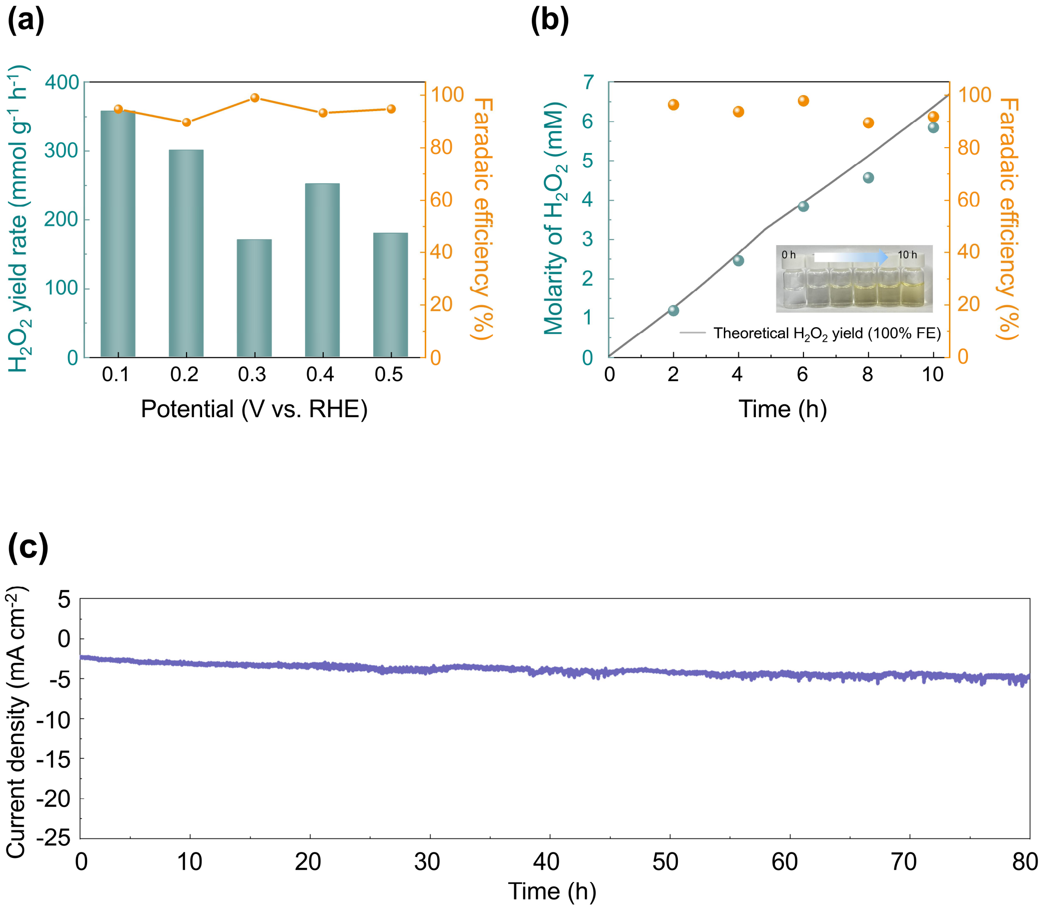

Figure 11

(a) H_2O_2 yield rates and FEs of the MoP pillars across voltages ranging from 0.1 0.5 V. The electrolyte was reacted with a 0.1 M $TiOSO_4$ solution to produce yellow-colored H_2TiO_4. (b) Theoretical H_2O_2 yield derived from the corresponding chronoamperometry curve, alongside the detected H_2O_2 molarity and calculated FE over 10 h at 0.1 V. The inset image illustrates the color change of the reaction mixture over time (left to right). (c) Long-term chronoamperometry of the MoP pillars at 0.1 V for 80 h.

3.3.5 Summary of Facet-Dependent Electrochemical Behavior

The electrocatalytic performance of MoP single crystals was strongly influenced by their exposed crystallographic facets. MoP pillars exposing the $(10\bar{1}0)$ facet exhibited significantly higher H_2O_2 selectivity, kinetic activity, and intrinsic site-specific performance compared to (0001) facet nanoplates. These advantages were consistently observed across both transient RRDE measurements and long term continuous electrosynthesis, confirming the $(10\bar{1}0)$ facet as more favorable for the $2e^-$ ORR pathway. This facet dependent behavior highlights the importance of precise surface engineering in optimizing the activity, selectivity, and durability of MoP based electrocatalysts.

3.4 DFT Calculation Results

Density functional theory (DFT) calculations were performed to uncover the facet dependent catalytic behavior of MoP single crystals. Under phosphorus rich conditions, the surface free energy of several low index planes was evaluated, and the P-terminated (0001) surface was identified as the most thermodynamically stable. This explains the preferential nucleation of MoP on this facet during synthesis, as illustrated by the surface energy comparison in Figure 12. To investigate how growth conditions influence morphology, the diffusion barrier of a Mo adatom was calculated for the stepped (0001) surface. The barrier was found to be 2.1 eV. Based on this, lateral diffusion at 900°C is estimated to be approximately 70 times faster than at 700°C, indicating that high temperatures promote in plane crystal growth and the formation of nanoplate morphologies with dominant (0001) facets. In contrast, lower temperatures limit surface mobility, directing growth vertically and favoring exposure of the $(10\bar{1}0)$ facet in pillars. This trend aligns with the experimentally observed shape evolution and diffusion-driven morphology, as shown in Figure 13.

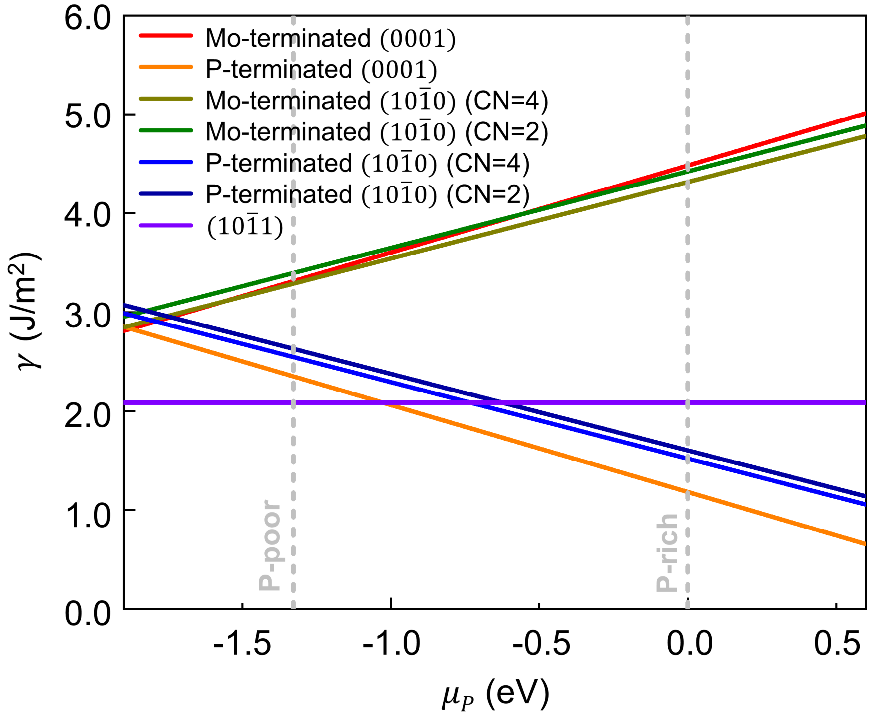

Figure 12

Surface free energies of MoP as a function of the chemical potential of P, with different orientations, terminations and coordination numbers.

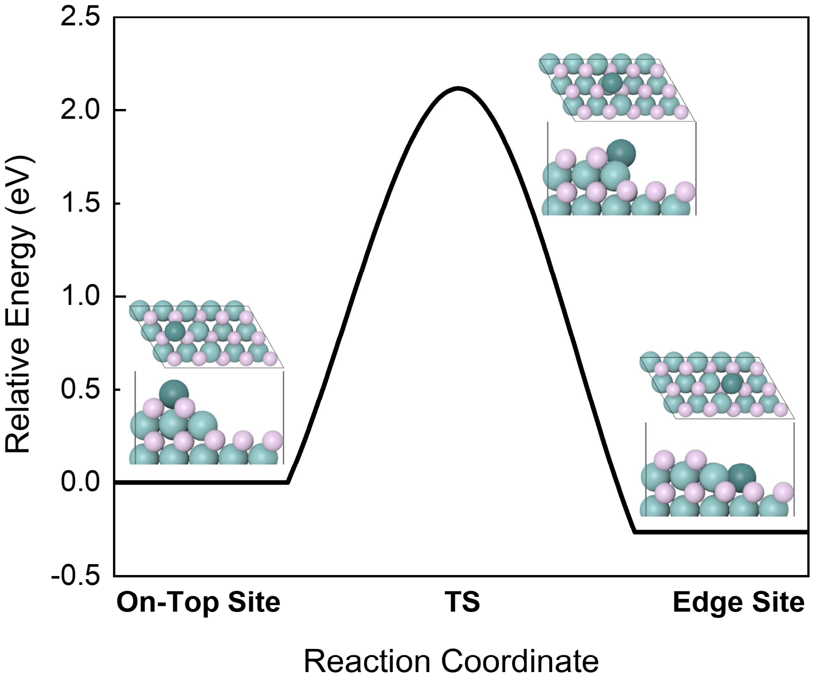

Figure 13

DFT-calculated diffusion energy barrier of a Mo adatom on the (0001) surface of MoP. The energy profile represents the migration of a Mo adatom from the terrace to a lower step edge, illustrating the energy barrier for lateral growth on the (0001) surface.

These facet specific growth directions are further illustrated in Figure 14, which presents top and side views of atomic configurations for the P-terminated (0001) and $(10\bar{1}0)$ surfaces. Teal and pink spheres indicate Mo and P atoms, respectively, highlighting the distinct atomic arrangements that govern their morphological and catalytic behavior.

The electrocatalytic implications of these facets were explored through calculated free energy profiles for both the two-electron and four-electron oxygen reduction reaction pathways. As shown in Figures 15a and 15b, the $(10\bar{1}0)$ facet exhibited a lower overpotential for H_2O_2 formation, requiring only 1.00V compared to 1.26V on the (0001) facet. This suggests that the pillars more effectively facilitate the two-electron pathway for selective hydrogen peroxide production.

To explain this trend at the electronic level, crystal orbital Hamilton population (COHP) analysis was performed. The OOH intermediate exhibited a weaker bonding interaction with the $(10\bar{1}0)$ facet, as reflected by its less negative integrated COHP value relative to that of the (0001) facet. This result is illustrated in Figure 16a, which compares the COHP plots of MoP nanoplate and pillar. Projected density of states (PDOS) analysis further revealed that the Mo-d band center on the $(10\bar{1}0)$ facet lies deeper in energy than on the (0001) facet, as illustrated by the PDOS plots in Figure 16b for the nanoplate and Figure 16c for the pillar. This electronic configuration reduces orbital overlap with OOH*, weakening adsorption and promoting intermediate desorption.

Collectively, these computational results clarify how facet-dependent surface energetics, diffusion driven morphology, and intermediate binding strength work in concert to enhance the $2e^-$ ORR activity of MoP single crystals exposing the $(10\bar{1}0)$ facet.

(0001) **P-terminated nanoplate**

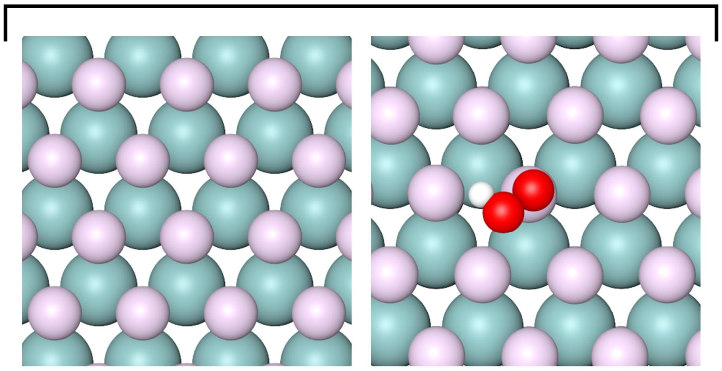

$(10\bar{1}0)$ **P-terminated pillar**

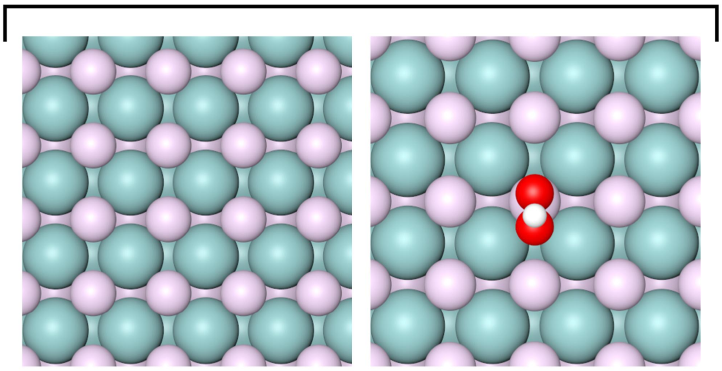

Figure 14

DFT analysis of facet-dependent catalytic performance of MoP, showing atomic configurations of bare and OOH-adsorbed phosphorus-terminated surfaces for both nanoplate and pillar morphologies.

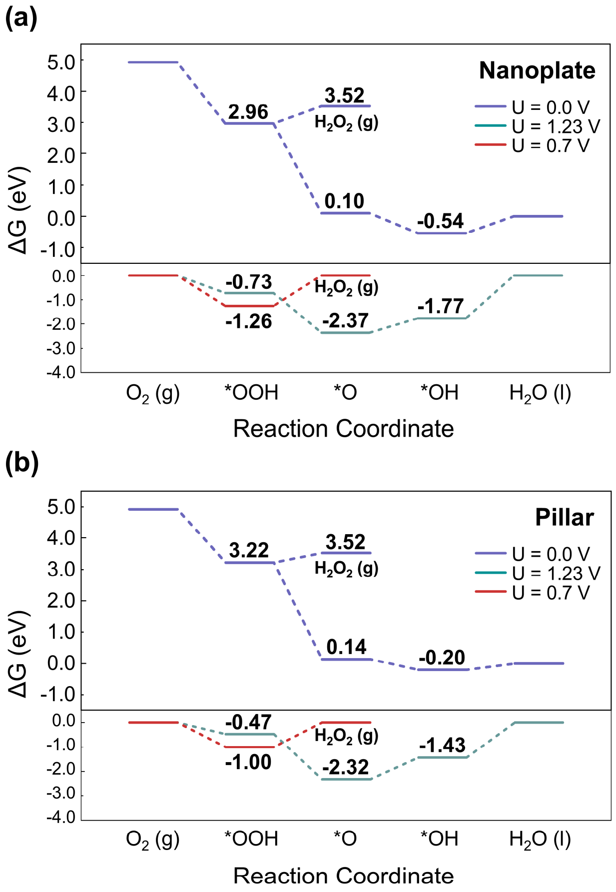

Figure 15

Calculated Gibbs free energy diagrams for the $2e^-$ and $4e^-$ pathways on (c) the MoP nanoplate and (d) MoP pillar.

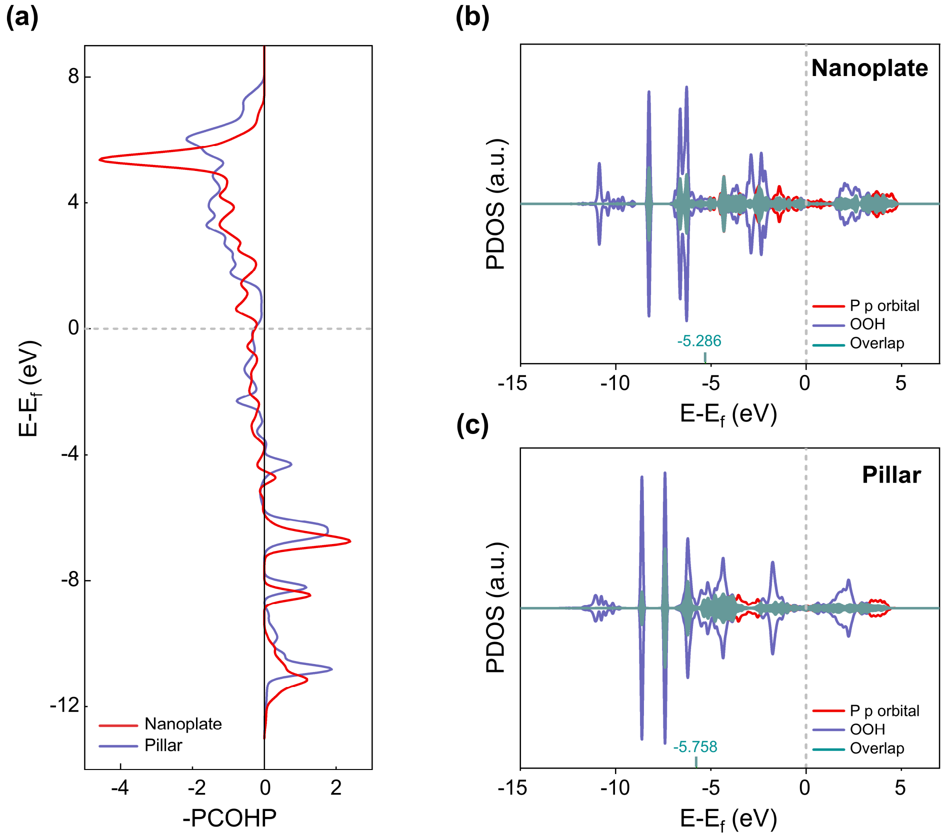

Figure 16

(a) COHP analyses of the MoP nanoplate and pillar. PDOS plots for (b) the nanoplate surface and (c) pillar surface with adsorbed OOH, highlighting overlapping regions.

Chapter 4. Conclusion

This study highlights the essential role of crystallographic facet control in optimizing the catalytic performance of molybdenum phosphide (MoP) single crystals for the two-electron oxygen reduction reaction ($2e^-$ ORR). Using a liquid metal assisted chemical vapor deposition method, well-defined crystal morphologies were selectively synthesized by adjusting the growth temperature, resulting in the exposure of either the thermodynamically stable (0001) facet or the kinetically favored $(10\bar{1}0)$ facet.

Comprehensive morphological characterization confirmed the high crystallinity and facet specificity of the resulting MoP crystals. Electrochemical analysis revealed that the $(10\bar{1}0)$ facet exhibited superior H_2O_2 selectivity, intrinsic activity, and favorable reaction kinetics relative to the (0001) facet. These experimental trends were further supported by density functional theory calculations, which demonstrated weaker OOH* adsorption and a lower overpotential on the $(10\bar{1}0)$ facet, providing a mechanistic explanation for its enhanced catalytic behavior.

These findings establish facet engineering as an effective strategy for tailoring the reactivity of transition metal phosphide electrocatalysts. The insights presented here offer a rational design framework for developing selective and efficient catalysts for electrochemical hydrogen peroxide production and related applications.

Bibliography

1. Pu, Z. *et al.*Transition metal phosphides: activity origin, energy related electrocatalysis applications, and synthetic strategies. *Adv. Funct. Mater.*30, 2004009 (2020).

2. Yu, F. *et al.*High-performance bifunctional porous non-noble metal phosphide catalyst for overall water splitting. *Nat. Commun.*9, 2551 (2018).

3. Yan, X. *et al.*An electron-hole rich dual-site nickel catalyst for efficient photocatalytic overall water splitting. *Nat. Commun.*14, 1741 (2023).

4. Kumar, N. *et al.*Extremely high conductivity observed in the triple point topological metal MoP. *Nat. Commun.*10, 2475 (2019).

5. Chi, Z. *et al.*Pressure-induced superconductivity in MoP. *npj Quantum Mater.*3, 28 (2018).

6. Lv, B. Q. *et al.*Observation of three-component fermions in the topological semimetal molybdenum phosphide. *Nature*546, 627 - 631 (2017).

7. Dada, O. O., Karimzadeh, S., Imoisili, P. E. & Jen, T.-C. Theoretical insights of electrocatalytic hydrogen evolution on MoP nanocrystal. *Int. J. Hydrogen Energy*48, 34634 - 34648 (2023).

8. Xiao, P. *et al.*Molybdenum phosphide as an efficient electrocatalyst for the hydrogen evolution reaction. *Energy Environ. Sci.*7, 2624 - 2629 (2014).

9. Huang, C.-J. *et al.*A review of modulation strategies for improving catalytic performance of transition metal phosphides for oxygen evolution reaction. *Appl. Catal. B Environ.*325, 122313 (2023).

10. Xu, J. *et al.*Trends in activity for the oxygen evolution reaction on transition metal (M= Fe, Co, Ni) phosphide pre-catalysts. *Chem. Sci.*9,

3470 - 3476 (2018).

11. Han, M., Wang, G., Zhang, H. & Zhao, H. Theoretical study of single transition metal atom modified MoP as a nitrogen reduction electrocatalyst. *Phys. Chem. Chem. Phys.*21, 5950 - 5955 (2019).

12. Zhou, Y., Yu, X., Sun, F. & Zhang, J. MoP supported on reduced graphene oxide for high performance electrochemical nitrogen reduction. *Dalt. Trans.*49, 988 - 992 (2020).

13. Kim, S.-J., Maligal-Ganesh, R. V, Mahmood, J., Babar, P. & Yavuz, C. T. Structural control over single-crystalline oxides for heterogeneous catalysis. *Nat. Rev. Chem.*1 - 18 (2025).

14. Chen, S., Xiong, F. & Huang, W. Surface chemistry and catalysis of oxide model catalysts from single crystals to nanocrystals. *Surf. Sci. Rep.*74, 100471 (2019).

15. Qu, R. *et al.*Antioil Ag3PO4 nanoparticle/polydopamine/Al2O3 sandwich structure for complex wastewater treatment: dynamic catalysis under natural light. *ACS Sustain. Chem. Eng.*6, 8019 - 8028 (2018).

16. Zhu, J. *et al.*Facile synthesis of a molybdenum phosphide (MoP) nanocomposite Pt support for high performance methanol oxidation. *Catal. Sci. Technol.*7, 5974 - 5981 (2017).

17. Wang, X. *et al.*A three-dimensional porous MoP@ C hybrid as a high-capacity, long-cycle life anode material for lithium-ion batteries. *Nanoscale*8, 10330 - 10338 (2016).

18. Cao, Y. *et al.*Facile synthesis of a molybdenum phosphide@ carbon nanocomposite as an advanced anode material for sodium-ion batteries. *New J. Chem.*43, 7386 - 7392 (2019).

19. Han, H. J. *et al.*Topological metal MoP nanowire for interconnect. *Adv. Mater.*35, 2208965 (2023).

20. Xia, C. *et al.*Confined local oxygen gas promotes electrochemical water oxidation to hydrogen peroxide. *Nat. Catal.*3, 125 - 134 (2020).

21. Hong, S., Kim, D., Kim, K.-J. & Park, J. Y. Facet-Controlled Cu2O Support Enhances Catalytic Activity of Pt Nanoparticles for CO Oxidation. *J. Phys. Chem. Lett.*14, 5241 - 5248 (2023).

22. Downes, C. A. *et al.*Controlled synthesis of transition metal phosphide nanoparticles to establish composition-dependent trends in electrocatalytic activity. *Chem. Mater.*34, 6255 - 6267 (2022).

23. Kalantar-Zadeh, K. *et al.*Emergence of liquid metals in nanotechnology. *ACS Nano*13, 7388 - 7395 (2019).

24. Taccardi, N. *et al.*Gallium-rich Pd - Ga phases as supported liquid metal catalysts. *Nat. Chem.*9, 862 - 867 (2017).

25. Daeneke, T. *et al.*Liquid metals: fundamentals and applications in chemistry. *Chem. Soc. Rev.*47, 4073 - 4111 (2018).

26. Cao, G. *et al.*Liquid metal for high-entropy alloy nanoparticles synthesis. *Nature*619, 73 - 77 (2023).

27. Wang, S. *et al.*A library of 2D electronic material inks synthesized by liquid-metal-assisted intercalation of crystal powders. *Nat. Commun.*15, 6388 (2024).

28. Gong, Y. *et al.*Growth of diamond in liquid metal at 1 atm pressure. *Nature*629, 348 - 354 (2024).

29. Wang, M. & Lin, Y. Gallium-based liquid metals as reaction media for

nanomaterials synthesis. *Nanoscale*16, 6915 - 6933 (2024).

30. Li, L., Zhang, Q., Geng, D., Meng, H. & Hu, W. Atomic engineering of two-dimensional materials via liquid metals. *Chem. Soc. Rev.*(2024).

31. Tian, Q. *et al.*Mesoporous carbon spheres with programmable interiors as efficient nanoreactors for H2O2 electrosynthesis. *Nat. Commun.*15, 983 (2024).

32. Sun, Y. *et al.*Boosting electrochemical oxygen reduction to hydrogen peroxide coupled with organic oxidation. *Nat. Commun.*15, 6098 (2024).

33. Zhang, C. *et al.*Trimetallic sulfide hollow superstructures with engineered D band center for oxygen reduction to hydrogen peroxide in alkaline solution. *Adv. Sci.*9, 2104768 (2022).

34. Kresse, G. & Furthmüller, J. Efficiency of ab-initio total energy calculations for metals and semiconductors using a plane-wave basis set. *Comput. Mater. Sci.*6, 15 - 50 (1996).

35. Kresse, G. & Hafner, J. Ab initio molecular dynamics for liquid metals. *Phys. Rev. B*47, 558 (1993).

36. Kresse, G. & Hafner, J. Ab initio molecular-dynamics simulation of the liquid-metal - amorphous-semiconductor transition in germanium. *Phys. Rev. B*49, 14251 (1994).

37. Perdew, J. P., Burke, K. & Ernzerhof, M. Generalized gradient approximation made simple. *Phys. Rev. Lett.*77, 3865 (1996).

38. Kresse, G. & Joubert, D. From ultrasoft pseudopotentials to the projector augmented-wave method. *Phys. Rev. b*59, 1758 (1999).

39. Blöchl, P. E. Projector augmented-wave method. *Phys. Rev. B*50, 17953

(1994).

40. Monkhorst, H. J. & Pack, J. D. Special points for Brillouin-zone integrations. *Phys. Rev. B*13, 5188 (1976).

41. Tian, X. *et al.*A DFT based method for calculating the surface energies of asymmetric MoP facets. *Appl. Surf. Sci.*427, 357 - 362 (2018).

42. Wang, C. *et al.*Facet engineering of advanced electrocatalysts toward hydrogen/oxygen evolution reactions. *Nano-micro Lett.*15, 52 (2023).

43. Jin Han, H. *et al.Unconventional Grain Growth Suppression in Oxygen-Rich Metal Oxide Nanoribbons. Sci. Adv*vol. 7 https://www.science.org (2021).

44. Lyu, F. *et al.*Two-dimensional mineral hydrogel-derived single atoms-anchored heterostructures for ultrastable hydrogen evolution. *Nat. Commun.*13, 6249 (2022).

논문개요

과산화수소(H_2O_2)는 소독, 정수, 화학 합성 등 다양한 분야에서 활용되는 필수 화학물질로, 그 수요가 꾸준히 증가하고 있다. 그러나 기존 산업 공정은 고온·고압 조건과 유기 용매를 필요로 하는 안트라퀴논 환원법에 의존하고 있어 에너지 소모와 공정상의 비효율성이 크다. 이를 대체할 수 있는 2전자 산소 환원 반응($2e^-$ ORR)에 기반한 전기화학적 H_2O_2 합성 기술이 주목받고 있으나, 높은 선택성과 효율을 동시에 갖춘 촉매 개발이 여전히 과제로 남아 있다. 몰리브덴 인화물(MoP)은 전기전도성과 화학적 안정성이 뛰어나 유망한 후보 소재로 평가받고 있으나, 기존 합성법은 다결정 또는 비정질 상태의 시료를 주로 생성하며, 결정면 제어가 어렵고 성장 속도가 느리다는 한계가 있다. 본 연구에서는 갈륨 기반 액체금속을 반응 매질로 활용한 화학 기상 증착(CVD) 공정을 통해 고결정성 MoP 단결정을 합성하였으며, 합성 온도 조절을 통해 결정면 방향을 정밀하게 제어하였다. 이를 통해 (0001) 면을 노출한 판상형 구조와 $(10\bar{1}0)$ 면을 노출한 기둥형 구조를 각각 선택적으로 구현하였으며, 두 구조는 형태학적으로 뚜렷한 차이를 보였다. 전기화학 분석 결과, $(10\bar{1}0)$ 면을 노출한 시료는 상대적으로 높은 과산화수소 선택성을 나타내었으며, 이는 결정면에 따른 반응 경로 차이에 기인하는 것으로 확인되었다. 본 연구는 결정면 제어가 가능한 MoP 단결정 합성법을 제시하였으며, 이는 기존의 구조적 제약을 극복하고 MoP 기반 $2e^-$ ORR 촉매의 설계와 활용 가능성을 근본적으로 확장한다.